

Measuring Micrometer-Level Vibrations with mmWave Radar

Junchen Guo, *Member, IEEE*, Yuan He, *Senior Member, IEEE*, Chengkun Jiang, *Member, IEEE*, Meng Jin, *Member, IEEE*, Shuai Li, *Member, IEEE*, Jia Zhang, *Member, IEEE*, Rui Xi, *Member, IEEE*, Yunhao Liu, *Fellow, IEEE*

Abstract—Vibration measurement is a crucial task in industrial systems, where vibration characteristics reflect health conditions and indicate anomalies of the devices. Previous approaches either work in an intrusive manner or fail to capture the micrometer-level vibrations. In this work, we propose mmVib, a practical approach to measure micrometer-level vibrations with mmWave radar. First, we derive a metric called *Vibration Signal-to-Noise Ratio* (VSNR) that highlights the directions of reducing measurement errors of tiny vibrations. Then, we introduce the design of mmVib based on the concept of *Multi-Signal Consolidation* (MSC) for the error reduction and multi-object measurement. We implement a prototype of mmVib, and the experiments show that it achieves 3.946% relative amplitude error and 0.02487% relative frequency error in median. Typically, the average amplitude error is only $3.174\mu m$ when measuring the $100\mu m$ -amplitude vibration at around 5 meters. Compared to two existing mmWave-based approaches, mmVib reduces the 80th-percentile amplitude error by 69.21% and 97.99% respectively.

Index Terms—Wireless Sensing, Millimeter Wave, Vibration Measurement.

1 INTRODUCTION

VIBRATION of industrial devices is generally the most common indicator that reflects their internal states. Damage or malfunction of the devices usually leads to abnormal changes in their vibration characteristics, e.g., amplitude and frequency. Therefore, vibration measurement is a crucial task in various industrial scenarios for anomaly detection, fault diagnosis, and life prediction [3], [5].

Conventional approaches for vibration measurement are based on specialized sensors or optical devices. Piezoelectric [1] and eddy-current [10] sensors are commonly used to provide accurate vibration measurement, but they need to be installed on the vibration source's surface, which could introduce non-trivial deployment and maintenance costs. Laser vibrometer is a promising non-contact solution for high-accuracy vibration measurement [11], [19]. However, its high device cost might prohibit the large-scale deployment. Recently, low-cost ranging LiDAR sensors [18], [34] are used to measure vibration signals. But their relatively limited range resolution and sample rate bring many challenges when restoring vibration signals.

With the rapid progress in wireless sensing, recent works exploit *Radio Frequency* (RF) signal [28], [30], [32], for vibration measurement. The vibrating object is a physical reflector of the wireless signal so that its vibration changes the propagation distance of the reflected signal. By analyzing the phase of the reflected signal, one can obtain the vibration characteristics or further restore the vibration signals. Compared to conventional approaches, wireless-sensing-based

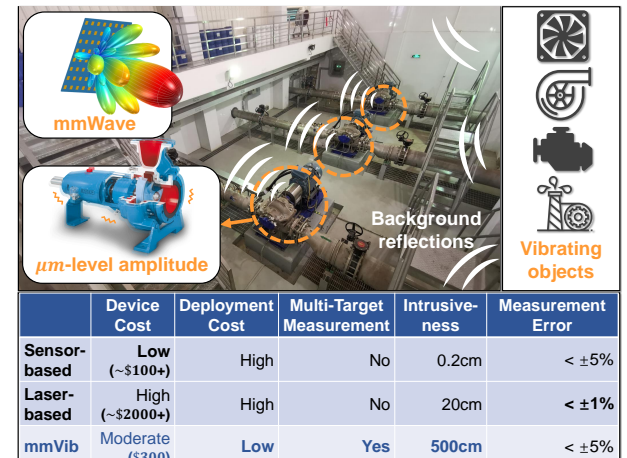


Fig. 1. Vibration measurement with mmVib

measurement is low-cost and easy to deploy and maintain in practice. However, according to the translation relationship from the micro displacement to the signal phase, the measurement precision is basically proportional to the signal wavelength, making it very challenging for conventional RF technologies like 915MHz RFID or 2.4GHz WiFi to perceive micro mechanical vibrations in industry.

Owing to the short wavelength, mmWave is a more promising technology for measuring micro displacements. Recent works use mmWave for high-precision tracking [29], hand gesture and human activity recognition [8], [14], object imaging and recognition [35], [36], localization and map construction [7], [15], [17], vital signal monitoring [4], [16], [33], noise-resistant speech sensing [31] and water-to-air wireless communication [25]. However, those approaches cannot be directly applied in the vibration measurement in industrial scenarios due to the following challenges.

• J. Guo, Y. He, C. Jiang, M. Jin, S. Li, J. Zhang, R. Xi and Y. Liu are with the School of Software and the Automation Department, Tsinghua University, Beijing, China. E-mail: juncguo@gmail.com, heyuan@mail.tsinghua.edu.cn, ahczjck@gmail.com, jinm@sjtu.edu.cn, lis20@mails.tsinghua.edu.cn, j-zhang19@mails.tsinghua.edu.cn, ruix.ryan@gmail.com and yunhao.liu@gmail.com.

First, the vibrations of industrial devices are often at the μm level. Although mmWave has a higher displacement sensitivity than other RF technologies, the phase changes caused by such tiny vibrations are easily affected by the noise. Second, a typical scenario shown in Fig. 1 illustrates that industrial environments are often multipath-rich. Although mmWave has a better directionality than conventional wireless signals, the received signal is still a mix of the signals reflected from both the vibrating objects and ambient reflectors. Therefore, the vibration-induced phase changes of the received mmWave signal are often obscured and distorted, making it extremely difficult to extract vibration signals accurately.

To address these challenges, we propose mmVib, a practical approach that measures μm -level vibrations with the commercial mmWave radar. mmVib inherits the characteristics of wireless sensing technologies, e.g., non-contact measurement manner, easy deployment and maintenance. And it also has the ability to provide a high-accuracy measurement that satisfies the μm -level requirement.

In this paper, we first discuss the key factors that affect the vibration signal's measurement error to motivate our work. By analyzing the geometric features of the vibration reflection signal in the *In-phase and Quadrature* (IQ) domain, we derive a metric called *Vibration Signal-to-Noise Ratio* (VSNR) to generalize the impacts of vibration amplitude, SNR, and signal carrier frequency on the measurement error. Our simulation shows that the measurement error is inversely proportional to VSNR.

Then, we design mmVib that improves VSNR for accurate vibration measurements with the *Frequency-Modulated Continuous Wave* (FMCW) mmWave radar. mmVib adopts the concept of *Multi-Signal Consolidation* (MSC) that considers multi-chirp and multi-antenna properties to solve the challenges above. For the multi-chirp property, mmVib regroups the signal samples of one FMCW chirp to generate multiple virtual chirps. The virtual chirps with different carrier frequencies can provide a group of coherent observations on the same vibration signal, which significantly improves VSNR and reduces the measurement error. For the multi-antenna property, mmVib combines multiple RX-antenna inputs to distinguish between reflection signals from the vibrating objects and static clutters. Therefore, built upon MSC, mmVib can simultaneous provides accurate vibration measurements of multiple vibrating objects.

Last, We implement mmVib on a commercial mmWave radar and evaluate its performance in both lab and real-world environments. The results show that mmVib achieves 3.946% relative amplitude error and 0.02487% relative frequency error in median. Typically, the average amplitude error is only 3.174 μm when measuring the 100 μm -amplitude vibration at around 5 meters. Compared to two mmWave-based approaches, mmVib reduces the 80th-percentile amplitude error by 69.21% and 97.99% respectively.

2 RELATED WORKS

In this section, we review the related literature of mmVib.

RF-based vibration measurement. As mentioned before, RF technologies with longer wavelengths have lower sensitivity of micro displacements. For *Ultra-High-Frequency*

(UHF) RFID working at 900MHz, Tagbeat [32] manages to measure the vibration frequency of sub- cm -level vibrations. Following works like TagSound [13] that utilizes specialized hardware to sense the vibration signal embedded in higher-order harmonics and TagSMM [30] that leverages deployment-based calibration improves the sensitivity to sub-mm-level. Approaches like ART [28] and UWHear [27] use 2.4GHz WiFi or sub-10GHz UWB can sense sub-mm-level vibrations, but they merely focus on improving the through-wall measurement performance rather than increasing the sensitivity.

mmWave-based vibration measurement. With a mm -level wavelength, mmWave is naturally more suitable for μm -level vibration measurement [4], [16], [25], [33]. Ding *et al.* have proposed a theoretical signal model that translates the signal properties of FMCW chirps to the vibration parameters [4]. However, without considering the multipath effect, the model fails to recover the vibration signal with the correct amplitude. To overcome the above problem, Mikhelson *et al.* analyze the reflection signal's geometric features in the IQ domain and introduce the geometric fitting method to quantify static multipath reflections [16]. However, the geometric features of tiny vibrations are less distinctive, which degrades the fitting process's performance. To deal with tiny vibrations, several approaches try to combine multiple coherent observations of the same vibration signal to magnify the geometric features, and improve the fitting performance [2], [12]. However, their realizations require specialized hardware, e.g. digital phase shifter [2] or *Orthogonal Frequency Division Multiplexing* (OFDM) radar [12].

In this work, we also focus on improving tiny vibration measurement performance with multiple coherent observations. Different from the above approaches, we theoretically analyze why multiple coherent observations reduce the measurement error as our motivation (§3) and provide a purely signal processing based solution that can be applied to commercial mmWave radars (§4)

3 MEASUREMENT ERROR AND VSNR

In this section, we first introduce the basic signal model of the vibration reflection signal (§3.1), then formulate the problem of the vibration measurement based on the geometric fitting (§3.2), and finally propose the definition of VSNR and describe its impact on the measurement error (§3.3).

3.1 Vibration Reflection Signal Model

Given a vibrating target at the distance $D(t)$ from the mmWave radar, $D(t)$ can be represented as $D(t) = D_0 + x(t)$ where D_0 is the constant object-radar distance and $x(t)$ is the vibration signal to be measured. If a *Continuous Wave* (CW) signal $S_{\text{TX}}(t) = e^{j2\pi f_c t}$ with the carrier frequency f_c is sent towards this target, we will get the received signal $S_{\text{RX}}(t)$ and the demodulated signal reflection signal $S(t)$ as:

$$S_{\text{RX}}(t) = AS_{\text{TX}} \left(t - \frac{2D(t)}{c} \right) = Ae^{j[2\pi f_c t - 4\pi f_c \frac{D(t)}{c}]} \quad (1)$$
$$S(t) = S_{\text{TX}}(t)S_{\text{RX}}^*(t) = Ae^{4\pi f_c \frac{D(t)}{c}}$$

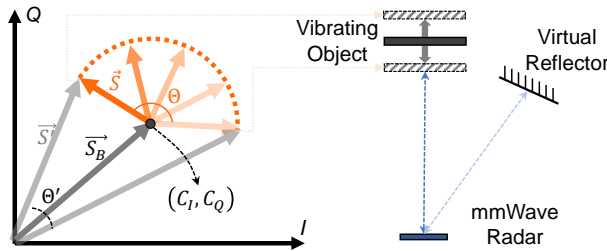


Fig. 2. Vibration reflection signal model

where A identifies the loss of the signal strength. Then, $\theta(t)$, the phase of $S(t)$, implies $x(t)$:

$$\theta(t) = 4\pi f_c \frac{D_0}{c} + 4\pi f_c \frac{x(t)}{c} \stackrel{\text{def}}{=} \theta_0 + \Delta\theta(t) \quad (2)$$

where θ_0 is the initial phase induced by D_0 and $\Delta\phi(t)$ is the phase variation. Then, $x(t)$ can be derived from $\Delta\phi(t)$ with the following equation:

$$x(t) = \frac{c}{4\pi f_c} \text{unwrap}(\Delta\theta(t)) \quad (3)$$

Where the *unwrap* function resolves the phase ambiguity. Eq. 3 tells that with the same precision of the phase reading, a higher carrier frequency deterministically results in a higher precision of the vibration signal.

3.2 Fitting-based Vibration Measurement

However, in practice, the receiving signal might contain other static reflections from ambient reflectors:

$$S'_{\text{RX}}(t) = Ae^{j[2\pi f_c t - 4\pi f_c \frac{D(t)}{c}]} + \sum_i A^{[i]} e^{j[2\pi f_c t - 4\pi f_c \frac{D^{[i]}}{c}]} \quad (4)$$

Then, the demodulated signal can be revised as:

$$\begin{aligned} S'(t) &= Ae^{j4\pi f_c \frac{D(t)}{c}} + \sum_i A^{[i]} e^{j4\pi f_c \frac{D^{[i]}}{c}} \\ &= Ae^{j4\pi f_c \frac{D(t)}{c}} + A_B e^{j4\pi f_c \frac{D_B}{c}} \stackrel{\text{def}}{=} S(t) + S_B \end{aligned} \quad (5)$$

In Eq. 5, all the static background reflections are regarded as one composite reflection S_B from one single virtual reflector, where D_B and A_B represent the distance from the virtual reflector to the radar and the signal strength of $S_B(t)$, respectively. Since the vibration signal $x(t)$ only lies in the phase of $S(t)$, our goal is to identify the value of S_B and eliminate it with $S(t) = S'(t) - S_B$.

The basic idea of deriving S_B from $S'(t)$ is to explore the geometric features of $S'(t)$ in the IQ domain. Fig. 2 displays the vector form of the signal superimposition: $\vec{S}' = \vec{S} + \vec{S}_B$. \vec{S} rotates with the object's vibration, and therefore \vec{S}' keeps synchronization with \vec{S} in the rotation frequency. Under this circumstance, the end of \vec{S}' moves along an arc of a circle whose (i) central angle $\Theta = 8\pi f_c \frac{X}{c}$ where $X = |x(t)|$ stands for the vibration amplitude, (ii) radius A represents the strength of the vibration reflection signal $S(t)$, and (iii) center coordinate (C_I, C_Q) is exactly the value of \vec{S}_B , i.e. $S_B = C_I + jC_Q$. Thus, the most intuitive way to determine (C_I, C_Q) is to fit a circle from the signal samples of $S'(t)$ and find its center coordinate [16].

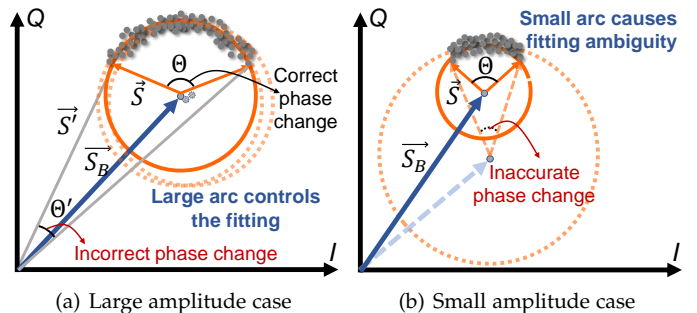


Fig. 3. Practical signal fitting under different vibration amplitudes

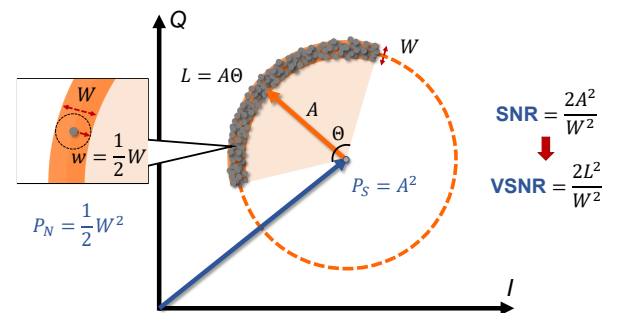


Fig. 4. VSNR Definition

Nevertheless, the samples of $S'(t)$ contains non-negligible noise in practice. When its SNR is limited by the transmitting power, the TX and RX antenna gain, the round-trip propagation distance, and the *Radar Cross Section* (RCS) of the vibrating object, the performance of the signal fitting degrades. Fig. 3 shows that under similar SNR, a large signal arc controls the fitting process and outputs a correct and accurate result. In contrast, a small signal arc causes fitting ambiguity and induces inaccuracy.

3.3 Vibration Signal-to-Noise Ratio

The analyses in §3.1 and §3.2 tell us that three critical factors, *carrier frequency* f_c , *vibration amplitude* X and *SNR*, determine the performance of the signal fitting and thus the measurement error of the vibration signal. Actually, we can derive a unified metric called *VSNR* from the geometric perspective in the IQ domain to generalize their relationships.

Our basic idea is that a longer arc length $L = A\Theta$ and a thinner arc width W make the arc shape more distinctive, further improving the signal fitting and then reducing the measurement error. First, the impact of carrier frequency f_c and vibration amplitude X is contained in Θ , since $\Theta = 8\pi f_c \frac{X}{c}$. Second, the impact of SNR can be quantified with the circle radius A and arc width W , as shown in Fig. 4. The signal power P_S can be deemed as the square of A (the signal strength), i.e. $P_S = A^2$. Since the average power of the zero-mean real additive Gaussian noise equals its variance w^2 , the complex noise power P_N can be represented as the aggregation of I channel and Q channel, i.e. $P_N = 2w^2$ [26]. If we define the arc width W as the double of the standard deviation w , SNR can be represented as:

$$\text{SNR} = \frac{P_S}{P_N} = \frac{A^2}{2(\frac{1}{2}W)^2} = \frac{2A^2}{W^2} \quad (6)$$

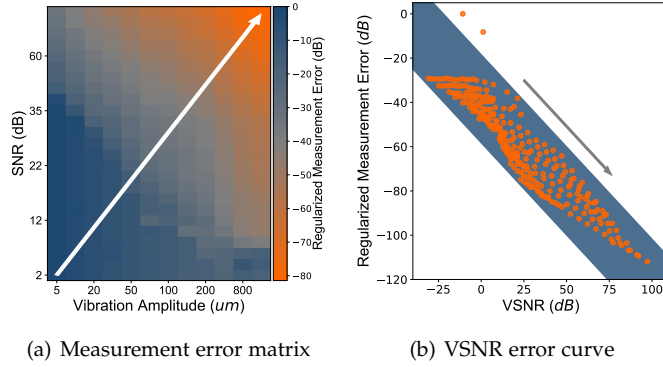


Fig. 5. Simulation results about VSNR and measurement errors

Then, by replacing A with $L = A\Theta$ in Eq. 6, we can represent the impacts of f_c , X and SNR within one single metric named *Vibration Signal-to-Noise Ratio* (VSNR):

$$\text{VSNR} = \frac{2L^2}{W^2} = \text{SNR} \cdot \Theta^2 = \text{SNR} \cdot \left(\frac{8\pi f_c X}{c} \right)^2 \quad (7)$$

Next, given a large carrier frequency f_c , e.g. 77GHz in our implementation, we run a simulation to study the relationship between VSNR and the measurement error. We count the measurement errors of the fitting-based approach as illustrated in §3.2 under different amplitude ($5 \sim 1600\mu\text{m}$) and SNR ($2 \sim 80\text{dB}$) settings. Here, the measurement error E is defined as the relative amplitude estimation error $E = |X_{\text{measured}} - X|/X$. Fig. 5(a) shows the average measurement errors in the regularized dB form, where the arrow denotes that E basically decreases with the increase of SNR and X . Moreover, if we compute the VSNR of each measurement setting, i.e., each cell in Fig. 5(a), we can directly visualize the relationship between E and VSNR. The so-called VSNR error curve is shown in Fig. 5(b). This figure further demonstrates that the log-scale measurement error of the fitting-based vibration signal extraction is basically inversely proportional to VSNR:

$$\log(E) \propto -\text{VSNR} \quad (8)$$

Eq. 7 and Eq. 8 together imply the interchangeability of the critical factors underlying VSNR. For instance, if we want to prolong the measurement distance of a tiny vibration without sacrificing accuracy, we have to keep VSNR unchanged by increasing the power of the vibration reflection signal. Moreover, Eq. 8 suggests that improving VSNR can reduce the measurement error, which acts as the basic principle of mmVib's design introduced next.

4 MMVIB DESIGN

4.1 Overview

To accurately measure the vibration signals of multiple vibrating objects with commercial mmWave radar, mmVib adopts the concept of *multi-signal consolidation*: (i) it leverages the *multi-chirp property* to improve overall VSNR and reduce the measurement error, and (ii) it leverages *multi-antenna property* to distinguish vibration signals from different vibrating objects. The following 4-step workflow of mmVib is illustrated in Fig. 6.

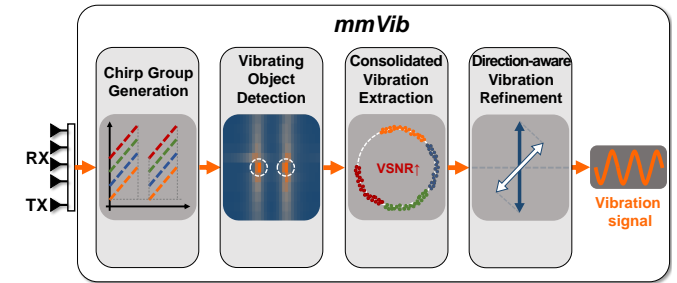


Fig. 6. Overview of mmVib

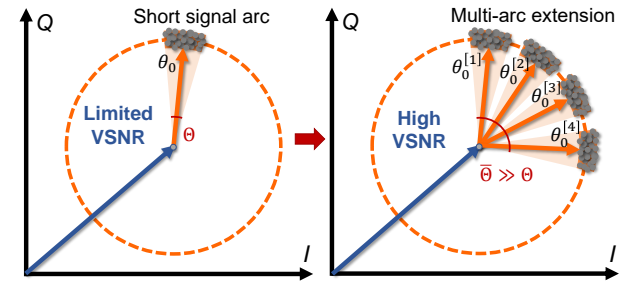


Fig. 7. Improving VSNR through multi-arc extension

- **Chirp Group Generation (CGG):** CGG takes the raw samples of mmWave FMCW chirp signals as inputs and generates a group of virtual chirps with different carrier frequencies to increase VSNR.
- **Vibrating Object Detection (VOD):** VOD takes the multi-chirp reflection signals from multiple RX antennas as inputs and analyzes their Range-Angle spectrum to distinguish the reflection signals from vibrating objects.
- **Consolidated Vibration Extraction (CVE):** CVE takes the reflection signals from vibrating objects as inputs and extracts the vibration signal. To reduce measurement errors, it combines the observations from multiple chirps to form a signal arc with more distinctive shape features.
- **Direction-aware Vibration Refinement (DVR):** DVR takes the measured vibration signal and corresponding Angle-of-Arrival (AoA) of the vibrating object as inputs and refines the vibration-amplitude estimation.

4.2 Chirp Group Generation

Since $\text{VSNR} = \text{SNR} \cdot \Theta^2$, the straightforward idea of improving VSNR is to extend the signal arc, i.e. extending Θ , as shown in Fig. 7. Suppose we can simultaneously send multiple signals with different carrier frequencies $f_c^{[g]}$, $g \in [1, G]$, we can get several short signal arcs with different initial rotating directions $\theta_0^{[g]}$ which together form a large signal arc with the significantly higher VSNR. However, without the help of specialized hardware [12], it's a non-trivial task to enable the commercial FMCW radar with this capability. Therefore, we introduce the novel technique CGG that creates a group of virtual FMCW chirps with different carrier frequencies without any hardware modification.

Original FMCW Range-FFT Process: Fig. 8(a) shows the waveform of FMCW chirp signals, which translates the frequency difference between TX and RX signals to the round-trip Time-of-Flight (ToF). Similar to Eq. 1, the fre-

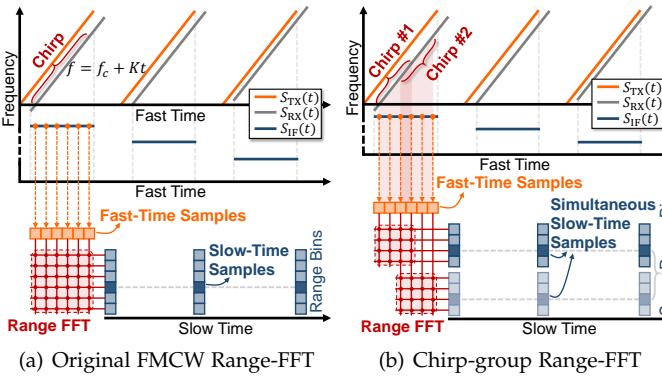


Fig. 8. Illustration of chirp group generation module

quency difference is perceived by analyzing the *Intermediate Frequency* (IF) signal after the TX-RX mixture [23]:

$$\begin{aligned} S_{\text{TX}}(t) &= e^{j(2\pi f_c t + \pi K t^2)} \\ S_{\text{RX}}(t) &= A S_{\text{TX}}(t - \frac{2D(t)}{c}) \\ \xrightarrow{\text{Mixture}} S_{\text{IF}}(t) &= S_{\text{TX}}(t) S_{\text{RX}}^*(t) \approx A e^{j4\pi(f_c + Kt)\frac{D(t)}{c}} \end{aligned} \quad (9)$$

, where f_c and K are the starting (i.e., carrier) frequency and the chirp slope of FMCW chirp, respectively.

In the front-end of the commercial mmWave radar, it first performs the analog TX-RX mixture and then obtains the so-called *fast-time samples* of $S_{\text{IF}}(t)$ whose sampling rate is about several MHz [24]. In practice, there exist reflected signals from different distances, which cause different frequency components in $S_{\text{IF}}(t)$. In order to extract the reflection signal from a specific distance, a *Range-FFT* operation [4], [23] is conducted on the fast-time samples within one chirp period. As shown in Fig. 8(a), this operation converts the time-domain samples to the range-domain samples. Since the elapsed time T of one chirp is only about 0.1ms, we assume the reflectors from a certain range bin keep static and only consider their movements across consecutive chirps. Therefore, we pick up one sample from a certain range bin in the Range-FFT result of each chirp and combine them to form a *slow-time* sample sequence of about 10kHz sampling rate. Denoting the fast and slow time by t and n respectively, the Range-FFT operation can be concluded as:

$$S_{\text{IF}}(nT + t) \stackrel{\text{def}}{=} S_{\text{IF}}(n, t) \xrightarrow{\text{Range-FFT}} S(n) = A e^{j4\pi f_c \frac{D(n)}{c}} \quad (10)$$

Note that, despite the time symbols, the right side of Eq. 10 is the same as Eq. 1 and so in the following analyses.

Chirp-group Range-FFT Process: Nevertheless, extracting the vibration signal $x(n)$ from a single-chirp observation $S(n)$ will experience a performance degradation under the condition of a low SNR or a tiny vibration amplitude. Then, *how to generate a chirp group that can simultaneously measure the same vibration as we expected?*

Our key insight is to rearrange the fast-time samples of $S_{\text{IF}}(t)$. Recall that the traditional Range-FFT operation uses all fast-time samples to generate one slow-time sample for each range bin. If we separate fast-time samples into different groups and perform Range-FFT in each group,

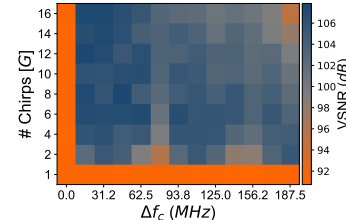


Fig. 9. CGG-VSNR matrix with different CGG parameters

we can obtain multiple synchronized slow-time samples for each range bin:

$$S_{\text{IF}}(n, t) \xrightarrow{\text{Chirp-group Range-FFT}} \left\{ S^{[g]}(n) \right\}_{g \in [1, G]} \quad (11)$$

Fig. 8(b) illustrates this process: we use a sliding window of size 4 on 6 fast-time samples and obtain two fast-time sample groups with a sliding step of 2 samples. This is equivalent to generate two shorter virtual chirps (Chirp #1, Chirp #2) with different starting frequencies from the original long chirp. The generated chirp group has two appealing characteristics of *coherence* and *difference*:

- Coherence:** Since the slow-time sampling rate is much lower than the fast-time one, the chirps in a group can be regarded as synchronized with each other.
- Difference:** Different chirps in the group start at different frequencies, which results in diversity among multiple observations of the same vibration.

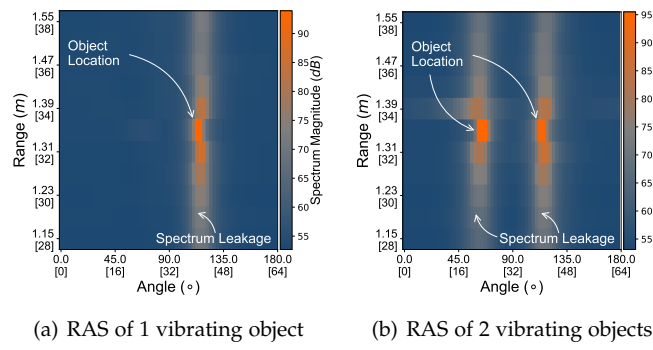
The impact of CGG on VSNR: Definitely, the second characteristic fulfills the multi-arc extension in Fig. 7. However, this operation extends Θ to $\bar{\Theta}$ at a non-negligible cost: the number of the fast-time samples of each virtual chirp is reduced and so is its SNR. Since $\text{VSNR} = \text{SNR} \cdot \bar{\Theta}^2$, this module can reduce the measurement error only when the finally induced VSNR increases.

To discuss the impact of CGG on VSNR, we have to consider its two key parameters: *number of chirps* (denoted by G) and *shifted frequency* (denoted by Δf_c) among two adjacent virtual chirps. G , Δf_c and the object distance D_0 together determine the value of the extended central angle $\bar{\Theta}$ of the large arc constructed by multi-chirp signals. Given the included angle between the initial rotating directions of two adjacent chirps as:

$$\Delta\Theta = \theta_0^{[g+1]} - \theta_0^{[g]} = \frac{4\pi D_0}{c} \left(f_c^{[g+1]} - f_c^{[g]} \right) = \frac{4\pi D_0}{c} \Delta f_c \quad (12)$$

, $\bar{\Theta}$ can be calculated as $\bar{\Theta} = \Theta + (G - 1)\Delta\Theta$ when $\Delta\Theta$ is a small acute angle as shown in Fig. 7. With a fixed distance D_0 , an increase of G and Δf_c basically leads to a larger $\bar{\Theta}$, but this operation decreases SNR since it reduces the number of fast-time samples of each virtual chirp. In order to determine whether CGG improves VSNR or not, we draw the CGG-VSNR matrix in Fig. 9, which implies that:

- The chirp-group Range-FFT ($G > 1$ or $\Delta f_c > 0.0\text{MHz}$) does improve VSNR, compared to the original Range-FFT ($G = 1$ or $\Delta f_c = 0.0\text{MHz}$).
- By carefully choosing the parameters G and Δf_c of CGG, we can obtain the highest VSNR that could lead to the smallest vibration measurement error.



(a) RAS of 1 vibrating object (b) RAS of 2 vibrating objects

Fig. 10. Illustration of vibration object detection module

However, increasing G also leads to an increased computation complexity. In practice, we first choose a small G , e.g., 4 to 8, considering the time cost. Then we determine the value of Δf_c that leads to a high VSNR according to the CGG-VSNR matrix corresponding to the vibrating object.

4.3 Vibrating Object Detection

Since the last module CGG provides the slow-time samples of the chirp-group Range-FFT from different range bins, VOD then detects the range bin(s) of the vibrating objects and extracts reflection signals from those objects. If multiple vibrating objects are located at the same range bin, mmVib uses the multi-RX array to provide the angular resolution and distinguish their reflection signals.

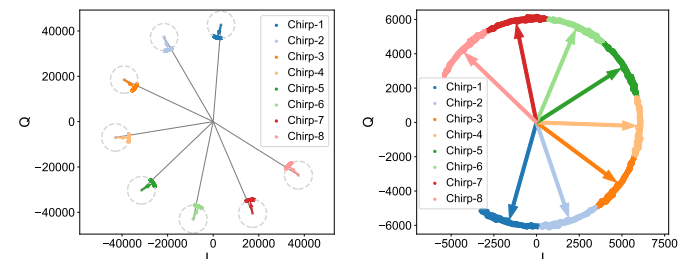
With multi-antenna inputs, the *Angle-FFT* operation is done to translate the antenna-domain signals to the angle-domain signals [23]. As in Range-FFT, the angle domain of Angle-FFT is also divided into several discrete *angle bins*. For the slow-time samples of Range-FFT $S(n), n \in [1, N]$, we denote the discrete range and angle bin by the subscripts r and a respectively, and denote the antenna index by another superscript $m, m \in [1, M]$. Then, Angle-FFT to extract the reflection signal from the location bin (r, a) is expressed as:

$$\left\{ S_r^{[m]}(n) = A e^{4\pi f_c \frac{D_r(n)}{c}} \right\}_{m \in [1, M]} \quad (13)$$

$$\xrightarrow{\text{Angle-FFT}} S_{r,a}(n) = A e^{4\pi f_c \frac{D_{r,a}(n)}{c}}$$

However, the resolution of the angle bin $\Delta a = \frac{2}{M \cos(a)}$ is around 30° for commercial 4-RX mmWave radar [23], which can hardly distinguish the reflection signals from adjacent vibrating objects. Thus, in order to solve this problem, we adopt the *Receiver Beamforming* (RBF) technology [22] instead of Angle-FFT. Like Angle-FFT, RBF also outputs the reflection signal from the discrete location bin (r, a) but achieves a much higher resolution in the angle domain.

RAS-based detection: To detect the location bins of vibrating objects, we run RBF on Range-FFT results of each range bin and plot the *Range-Angle Spectrum* (RAS) [22] as shown in Fig. 10. In this observation experiment, we place one vibrating object or two identical ones ($50\mu\text{m}$ amplitude and 50Hz frequency) in front of the mmWave radar and calculate corresponding RAS with *direct-current component removal* in Fig. 10(a) and 10(b) respectively. We can tell from the figures that, despite non-negligible spectrum leakage, the location bins of the vibrating objects have the highest energy in their local neighborhoods. Therefore, as done in



(a) Raw samples of 8 chirps (b) Translated samples of 8 chirps

Fig. 11. Observations of multi-chirp signals

multi-target tracking systems [9], we iteratively find the local peak with the highest energy until given numbers of vibrating objects are found. To enhance the system with more robustness, we inspect the 3×3 neighborhood of the local peak in our implementation.

MSC processing chain: For each detected location bin (r, a) , the MSC processing chain is summarized as:

$$\left\{ S_{\text{IF}}^{[m]}(n, t) \right\} \xrightarrow{\text{CGG}} \left\{ S_r^{[m,g]}(n) \right\} \xrightarrow{\text{VOD}} \left\{ S_{r,a}^{[g]}(n) \right\} \quad (14)$$

, where the dimension of $\left\{ S_{r,a}^{[g]}(n) \right\}, G \times N$, stands for N slow-time samples from G virtual chirps.

4.4 Consolidated Vibration Extraction

The CVE module extracts the vibration signal $x(t)$ from the multi-chirp observations $\left\{ S_{r,a}^{[g]}(n) \right\}$. To evaluate our insight that multi-chirp observations can extend the signal arc to improve VSNR, we visualize the processing results of a $100\mu\text{m}$ -amplitude and 50Hz -frequency vibration signal in Fig. 11(a). The vibration reflections (colored lines) rotate around their circle centers (grey dotted circles). However, the background reflections (grey lines) also rotate around the origin of coordinates. Thus, only when we find each reflection signal's correct circle center can we obtain the combined vibration reflection with a more distinctive arc shape. Fig. 11(b) shows the large signal arc formed by moving the circle centers to the origin of the coordinates. This acts as the basic idea of the CVE module:

- First, we estimate each chirp signal's background reflection through *basic circle fitting* step.
- Then, we use *consolidated circle fitting* step to generate a fitting constraint for each chirp signal that in turn improves the first step. The first two steps iteratively run until a perfect large arc is obtained.
- Finally, we extract the vibration signals from multi-chirp signals and aggregate the final measurement with the *vibration signal extraction* step.

Below are the details of the 3-step algorithm.

4.4.1 Step 1 - Basic Circle Fitting

Let $s_{g,n} = (\text{Re}(S_{r,a}^{[g]}(n)), \text{Im}(S_{r,a}^{[g]}(n))) \in \mathbb{R}^2$ be the n^{th} IQ samples from g^{th} chirp. For the g^{th} chirp, the fitting is turned into an optimization problem to obtain a circle with radius r_g and center $z_g = (z_{x_g}, z_{y_g})$ that minimizes the summed geometric distance from every sample to the circle:

$$z_g^*, r_g^* = \arg \min_{z_g, r_g} \sum_{n=1}^N (\|s_{g,n} - z_g\| - r_g)^2, g \in [1, G] \quad (15)$$

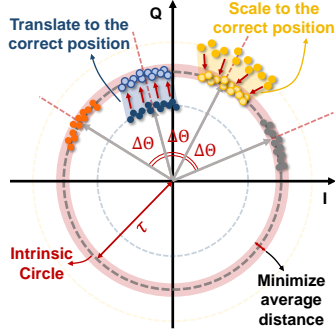


Fig. 12. Illustration of consolidated circle fitting module

It is a nonlinear least-square optimization problem and can be solved with the *Levenberg-Marquardt* (LM) algorithm [6]. However, when VSNR is low, the basic circle fitting is error-prone without a proper constraint on the radius.

4.4.2 Step 2 - Consolidated Circle Fitting

The first step gives a basic but not always accurate estimation of each chirp signal's background reflection. Therefore, combining multiple translated chirps signals after the background elimination probably won't form a perfect large arc as expected. Suppose the large arc falls on an *intrinsic circle*, Fig. 12 shows the two cases that each chirp signal might not necessarily fall on it: (i) *translation-needed case*: an improperly fitted radius will make the IQ samples of a chirp fall inside (blue ones) or outside the circle; (ii) *scaling-needed case*: a stronger or weaker signal strength of a chirp will make its IQ samples fall on other concentric circles of the intrinsic circle (yellow ones). Thus, we can get a perfect large arc by properly translating and scaling each chirp's IQ samples. We design the following consolidated circle fitting process:

- First, we eliminate the background reflection of each chirp signal. For the IQ samples of the g^{th} chirp $\{s_{g,n}\}_{n \in [1,N]}$, the elimination means subtracting the chirp signal by its center coordinate: $s'_{g,n} = s_{g,n} - z_g^*, n \in [1, N]$, where z_g^* is determined with step 1.
- Second, we resolve the scaling-needed cases by scaling the translated IQ samples to make the signal arcs of different chirps have identical arc length: $s''_{g,n} = \gamma_g \cdot s'_{g,n}, n \in [1, N]$, where the amount of the scaling γ_g is separately calculated for each chirp. We denote the radius of the scaled signal arc by r'_g , where $r'_g = \gamma_g \cdot r_g$.
- Third, we resolve the scaling-needed cases by determining the amount of the translation for each chirp to make its samples fall on the intrinsic circle. For each chirp signal, we derive its translation direction Δs_g as the unit vector of the vector from the origin of coordinates to the average sample point $\frac{1}{N} \sum_{n=1}^N s''_{g,n}$. Then, translating the chirp signal along Δs_g by the amount σ_g can be represented as: $\{s''_{g,n} + \sigma_g \cdot \Delta s_g\}_{n \in [1,N]}$. Denoting the radius of the intrinsic circle by τ , σ_g is actually determined by τ and r'_g , i.e. $\sigma_g = \tau - r'_g$. Then, there is only one variable τ left to make the scaled and translated chirp signal perfectly fall on the intrinsic circle.
- Finally, we search τ by minimizing the average geometric

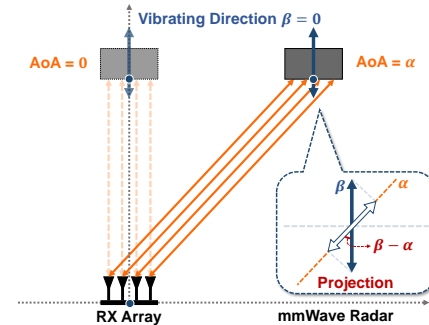


Fig. 13. Illustration of direction-aware vibration refinement module

distance of every chirp sample to the intrinsic circle:

$$\tau^* = \arg \min_{\tau} \frac{1}{GN} \sum_{g=1}^G \sum_{n=1}^N (\|s''_{g,n} + \sigma_g \Delta s_g\| - \tau)^2 \quad (16)$$

In order to avoid the above optimization problem from converging to local optima, we run the solver with multiple initial values of τ and select the best one as τ^* .

After finding the best radius of the intrinsic circle, τ^* , the expected radius for each chirp can be calculated with the inverse scaling: $r_g^* = \frac{\tau^*}{\gamma_g}$. Because the radius r_g^* will make the g^{th} chirp signal fall on the intrinsic circle, it can be set as a constraint of step 1 to better estimate its background reflection. Therefore, we iteratively run step 1 and step 2 until the relative change of the loss in Eq. 16 is less than a small threshold, e.g., 1%.

Denoting the time cost of each chirp signal's fitting process by I_1 and that of the fitting process for the intrinsic circle by I_2 , the total time cost of H -time iterations is $(G \cdot I_1 + I_2) \cdot H$. According to our experience, H is usually less than 3, i.e., the iteration converges very quickly. Then, the total processing time is mainly determined by the size of the chirp group G . The iteration outputs a more accurate estimation of $\{z_g^*\}_{g \in [1,G]}$ under low VSNR, which further reduces the measurement error of the vibration signal.

4.4.3 Step 3 - Vibration Signal Extraction

For g^{th} chirp, with the phase values of its translated sequence $\{\phi_{g,n} = \angle(s_{g,n} - z_g^*)\}_{n \in [1,N]}$, we obtain one measurement of the vibration signal $\{x_{g,n}\}_{n \in [1,N]}$:

$$x_{g,n} = \frac{c}{4\pi f_c^{[g]}} \text{unwrap}(\phi_{g,n}) - D_0, n \in [1, N] \quad (17)$$

where $f_c^{[g]}$ is the carrier frequency of g^{th} chirp. By aggregating all the measurements calculated with the chirp group, we get the final measurement $\{x_n\}_{n \in [1,N]}$. We use the *Inter-Quartile Mean* (IQM) aggregation algorithm, which calculates the truncated mean of the data within its inter-quartile range: $x_n = \text{IQM}(\{x_{g,n}\}_{g \in [1,G]}), n \in [1, N]$. Finally, the vibration amplitude and frequency of $\{x_n\}_{n \in [1,N]}$ are calculated to evaluate the performance of mmVib.

4.5 Direction-aware Vibration Refinement

Since mmWave radar can only sense the displacement along the *Line-of-Sight* (LoS) direction towards the vibrating objects, the CVE module's measurement is just a projection of

the vibration signal to this direction. Therefore, this DVR module exploits the multi-antenna property to recover the vibration signal along its real vibrating direction.

Denoting the AoA of the vibrating object and its real vibrating direction are α and β respectively, the measurement $\{x_n\}_{n \in [1, N]}$ is actually a projection of the vibration signal on an angle $\beta - \alpha$, as shown in Fig. 13:

$$x_n = x_n^* \cdot \cos(\beta - \alpha) \Rightarrow x_n^* = \frac{x_n}{\cos(\beta - \alpha)}, n \in [1, N] \quad (18)$$

where $\frac{1}{\cos(\beta - \alpha)}$ acts as a scaling factor to refine the vibration amplitude. In Eq. 18, β can be set to a constant through the deployment in practice, e.g., $\beta = 0$ in our experiments. We get α of the vibrating object at (r, a) with the multi-antenna property: $\alpha = a \cdot \Delta a$. A larger antenna array with more antennas can definitely lead to a better estimation of the final vibration. Moreover, it is also feasible to improve the result by combining multiple vibration measurements from multiple synchronized radars at different angles.

5 DISCUSSION

Next, we discuss the abilities and limitations of mmVib.

5.1 Multi-object Measurement

First, mmVib can measure multiple vibrating objects, but such ability is mainly limited by the hardware configuration of the mmWave radar. According to the relative position relationship between the mmWave radar and multiple vibrating objects, we classify the multi-object measurement situations into two categories: *objects at different range bins* and *objects at the same range bin*.

For the first category, it's easy for mmVib to distinguish their reflection signals through the Range-FFT process. In §6.4, our case study shows that we can configure the radar's deployment position so that multiple vibrating objects are located at different range bins. However, it is possible that we can't achieve this ideal deployment condition, and we have to deal with the second category that several vibrating objects fall into the same range bin.

In §4.3, we demonstrate that mmVib can clearly detect two vibrating objects at the same range bin and extract their reflection signals through RBF technologies. However, our evaluation shows only when the distance between the two vibrating objects is long enough, i.e., they have distinctive AoAs, can RBF works well in the signal separation. The resolution of the signal separation is fundamentally determined by the radar aperture's size, i.e., the number of RX antennas for the commercial mmWave radar working in the monostatic mode [22]. Therefore, to improve the multi-object measurement capability, one can port the processing pipeline of mmVib to a more powerful hardware platform.

5.2 NLoS Measurement

Second, mmVib has the limited capability of *None-Line-of-Sight* (NLoS) measurement. Due to the wireless and non-contact measurement scheme of mmVib, we have to consider whether it can work or not if the LoS path is blocked. Theoretically, mmWave signals with higher carrier frequencies than traditional RF technologies will go through more



(a) Measurement distance = 80cm (b) Measurement distance = 640cm

Fig. 14. Experiment setups and measurement results of mmVib

attenuation during the penetration. Thus, in the practical deployment of mmVib, we should avoid thick or metal blockages, e.g., walls and pillars. Fortunately, our evaluation in §6.3.1 shows that the performance of mmVib doesn't have a distinctive degradation when thin and non-metallic blockages exist. Therefore, we may enclose the mmWave radar board and its onboard antenna to improve their durability.

5.3 Impact of Dynamic-Multipath Interference

The capability of spatial signal separation of RBF also enables mmVib to be resilient to dynamic-multipath interference caused by walking people and running vehicles. Our evaluation in §6.3.3 shows that mmVib can well focus on the vibrating object as long as the LOS path is not blocked.

5.4 Impact of Phase Noise

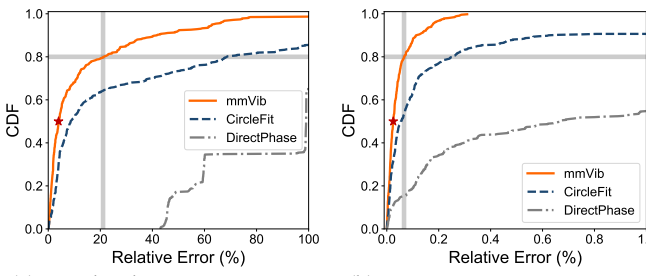
The phase noise, which stands for the short-term frequency instability of the signal caused by imperfection of manufacture, cascading propagation among RF devices, TX-RX leakage, etc., is often modeled as the composition of low-frequency flicker noise and high-frequency white noise [20]. The radar manufacturer provides a rough phase noise measurement about $-93\text{dBc}/\text{Hz}@1\text{MHz}$ offset along the $77 \sim 81\text{GHz}$ working band, which is quite small [24]. We also conduct an observation experiment to understand the practical phase noise of the mmWave radar. We place a still metal plate in front of the radar and collect its reflection signal for 10s (200 frames). The result shows that the impact of phase noise is reflected by the signal arc widened with *Additive White Gaussian Noise* (AWGN) and the initial angle of the reflection signal shifted by around 0.4363rad in a monotonous way. To deal the latter component, we process every frame separately to diminish the impact of the initial angle shift from 0.4363rad to $\frac{0.4363\text{rad}}{200} = 2.181e^{-3}\text{rad}$. The amplitude error induced by this component is calculated as:

$$\delta\Theta = \frac{8\pi f_c \delta X}{c} \Rightarrow \delta X = \frac{c\delta\Theta}{8\pi f_c} = 0.3381\text{um} \quad (19)$$

Therefore, we only address the negative impact of AWGN on the vibration measurement and manage to relieve it with the idea of chirp group consolidation.

6 EVALUATION

In this section, we introduce the implementation of mmVib and its evaluations in both our lab and a steel plant.



(a) Amplitude estimation errors (b) Frequency estimation errors

Fig. 15. Overall performance of vibration measurement

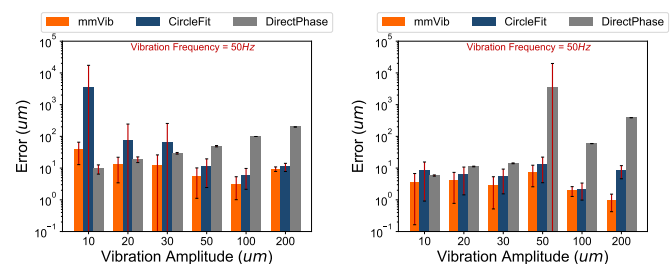
6.1 Implementation and Methodology

Implementation: We implement mmVib on a commercial mmWave radar, TI IWR1642 BoosterPack [24]. IWR1642 chip works on a 77GHz millimeter-wave frequency band ($77 \sim 81\text{GHz}$). It integrates 6 on-board antennas (2 TX antennas and 4 RX antennas). We let TX1 send the FMCW signal with 3.75GHz bandwidth, and RX1~RX4 receive the reflected signal. The raw sampling rate of the IF signals (i.e., fast-time sampling rate) is 3.43MHz. The chirp period and between-chirp idle time is 80 μs and 420 μs respectively, which together determine the chirp sampling rate (i.e. slow-time sampling rate) as $\frac{1}{(80+420)\mu\text{s}} = 2\text{kHz}$. Note 2kHz slow-time sampling rate can measure the vibration signal with $\leq 1\text{kHz}$ frequency. The raw fast-time samples are captured through a TI DCA1000EVM data acquisition board in a high-speed and real-time manner. The data processing coded in Python runs on a computer with an Intel i7-8565U processor and 16GB memory. The mmWave board costs \$299, while its core chip only costs \$40.

Experiment setting: The experiments are conducted in our lab and a steel plant. In the lab, we use the vibration calibrator to generate tunable vibrations with 20Hz to 500Hz ($\pm 1\%$) frequency and 5 μm to 500 μm ($\pm 1\%$) amplitude. These parameters describe the typical vibrations of industrial objects. When evaluating the impacts of these parameters, a vibration calibrator is placed in front of the radar as the vibrating object. When evaluating the multi-object measurement performance, we use two identical vibration calibrators. Fig. 14 shows the experiment setup in a hallway of $2.4\text{m} \times 10\text{m}$. The vibration calibrator is placed on a table while the mmWave radar is placed on a tripod. We evaluate mmVib in terms of vibration amplitude and frequency, measurement distance and angle, etc. For each setting, we collect at least 80 traces of raw mmWave data.

Comparisons: To evaluate the performance of mmVib, we choose two mmWave-based vibration measurement approaches introduced in previous sections as baselines: the phase-based method proposed in [4] (denoted by *DirectPhase*) and the basic fitting-based method proposed in [16] (denoted by *CircleFit*). To ensure fairness, these three approaches use the same data and the same pre-processing and post-processing methods.

Metrics: We consider the errors in amplitude and frequency estimation: the latter indicates the correctness of the measured vibration signals while the former stands for the accuracy. Moreover, we use the relative amplitude/frequency estimation error to unify the evaluation results under different settings.



(a) Lower VSNR (Dist. = 480cm) (b) Higher VSNR (Dist. = 160cm)

Fig. 16. Impact of vibration amplitude

6.2 Evaluation of Vibration Measurement

In this experiment, we evaluate the performance of mmVib and the other two approaches by changing the vibration amplitude (from 10 μm to 200 μm), frequency (from 20Hz to 400Hz), and the measurement distance (from 80cm to 640cm). The calibrator is placed directly in front of the radar with a vibrating direction along the radar's norm direction. In these cases, smaller amplitude and farther distance mean lower VSNR. Fig. 14 shows the raw slow-time samples, samples translated to the intrinsic circle, and extracted vibration signals under different VSNR conditions.

6.2.1 Overall performance

Fig. 15 shows the overall performance of mmVib, CircleFit and DirectPhase under all the measurement settings except for 10 μm -amplitude cases.

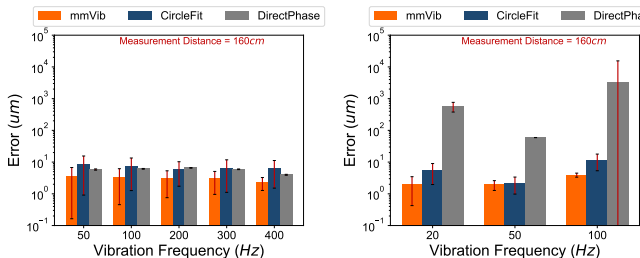
First, the red stars in the figures show that mmVib achieves 3.946% relative amplitude error and 0.02487% relative frequency error in median. This indicates that mmVib can correctly measure the vibration signal with high accuracy. Compared with the reported measurement accuracy of the traditional eddy-current displacement sensor ($< \pm 5\%$ error) [10] and laser displacement sensor ($< \pm 1\%$ error) [11], mmVib achieves the comparable measurement accuracy but is clearly superior in terms of the measurement distance, which significantly enhances the applicability in practice.

Second, the grey lines in the figures show that mmVib outperforms CircleFit and DirectPhase in both amplitude and frequency estimation. Compared to other two approaches, mmVib reduces the 80th-percentile amplitude error by 69.21% and 97.99% and reduces the 80th-percentile frequency error by 73.23% and 99.92%. Moreover, apart from measurement errors, mmVib also has smaller standard deviations, which stands for higher measurement stability and consistency.

Next, we examine the impact of different factors on the estimation accuracy (i.e., average error) and stability (i.e., error standard deviation) in Fig. 16-18 whose Y-axis is logarithmic-scale. Since the fitting-based approaches mmVib and CircleFit have shallow absolute frequency errors, we mainly focus on discussing their amplitude errors in the following evaluations.

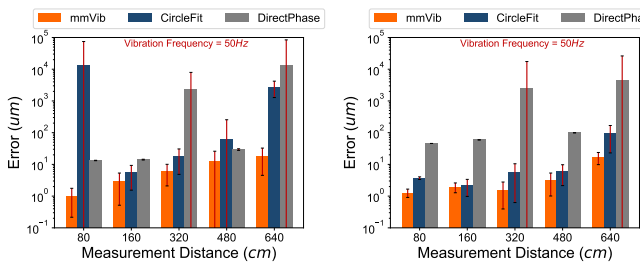
6.2.2 Impact of vibration amplitude

In this experiment, we keep the frequency to 50Hz and change the amplitudes from 10 μm to 200 μm at two distances 160cm and 480cm respectively. The results in Fig. 16 illustrates that: (i) mmVib can accurately measure the tiny



(a) Lower VSNR (Amp. = 10um) (b) Higher VSNR (Amp. = 100um)

Fig. 17. Impact of vibration frequency



(a) Lower VSNR (Amp. = 30um) (b) Higher VSNR (Amp. = 100um)

Fig. 18. Impact of measurement distance

vibrations at a relatively far distance: for the 160cm-30um case, it achieves an average amplitude error of 2.925um with a 2.408um standard deviation; for the 480cm-100um case, it achieves an average amplitude error of 3.174um with a 2.165um standard deviation. (ii) The comparisons among mmVib, CircleFit and DirectPhase demonstrate that the performances of two fitting-based approaches are generally proportional to VSNR, e.g., higher amplitudes and shorter distances lead to a finer measurement. Since CircFit can be easily affected by noises, the improvement of mmVib in the accuracy and stability is more significant when VSNR is lower. Meanwhile, DirectPhase has more inaccurate but more stable measurements as long as the slow-time samples are not close to the origin of the coordinate.

6.2.3 Impact of vibration frequency

In this experiment, we keep the distance to 160cm and change the frequencies from 20Hz to 400Hz at two amplitudes 10um and 100um respectively. Due to the power limitation, our calibrator cannot generate vibration signals of a large amplitude at a high frequency or a small amplitude at a low frequency. We can see from Fig. 17 that: (i) For lower-VSNR cases (10um-amplitude), mmVib achieves low amplitude errors at a large frequency range, i.e., 3.019um on average. Besides, samples with the same total sampling time contain more vibration periods for a higher frequency, which further reduces the measurement error. (ii) For higher-VSNR cases (100um-amplitude), mmVib also outperforms the other two approaches at different frequencies, but the performance gains are relatively smaller.

6.2.4 Impact of measurement distance

In this experiment, we keep the frequency to 50Hz and respectively measure 30um and 100um vibrations at a distance from 80cm to 640cm. We can see from Fig. 18 that: (i) mmVib works well at a relatively wide range of measurement distances. For instance, it achieves less than

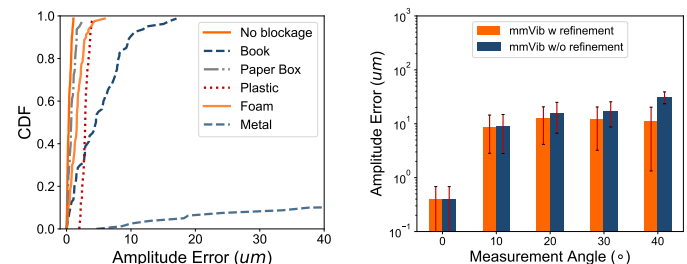


Fig. 19. Impact of blockage material.

Fig. 20. Impact of measurement angle.

5% relative amplitude estimation error when measuring 100um-amplitude vibrations at the range around 500cm, which satisfies the measurement requirements from real industries. (ii) Basically, the shorter the distance is, the finer measurement it provides. (iii) mmVib outperforms the other two approaches at all these distances.

6.3 Considerations of Practical Factors

Next, we evaluate the impact of several practical factors related to the applicability of mmVib in practice.

6.3.1 NLOS measurement

First, we evaluate the ability of mmVib to deal with LOS-path blockages. We set the vibration frequency and amplitude to 50Hz and 100um and keep the measurement distance as 100cm. We place blockage objects with different materials (paper box, plastic shell, foam block, thick book, and metal plate) in front of the mmWave radar (~ 50cm) and evaluate the amplitude errors.

The CDF plots in Fig. 19 show that (i) the metal materials will completely block the mmWave signal and make mmVib's measurements inapplicable; (ii) as long as the blockage objects are not particularly thick, mmWave can penetrate them, and the induced measurements achieve amplitude errors no more than 5um in most cases. Based on this result, we may enclose the mmWave board and its onboard antenna to improve the devices' durability.

6.3.2 Multi-angle measurement

Second, we evaluate the ability of mmVib to measure the vibrating object at different angles. As shown in Fig. 14(a), we keep the vibrating direction along the antenna array's norm direction and translate the calibrator to control the measurement angles from 0° to 40°. The vibration frequency and amplitude are set to 50Hz and 100um.

By comparing the performances of mmVib with and without the DVR module under different measurement angles, the results in Fig. 20 show that (i) the amplitude error increases with the measurement angle, since mmWave signals with less energy reflect back to the radar according to the principle of specular reflection; (ii) for different measurement angles, mmVib achieves the average amplitude error of 8.816um; (iii) The performance gain of DVR is more significant when the measurement angle is larger, e.g., 31.22um → 10.82um in the 40° case.

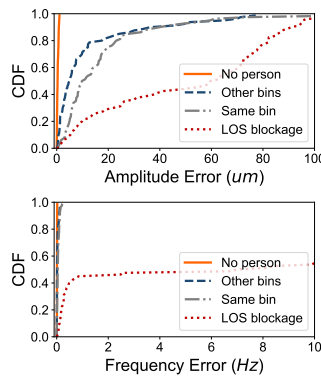


Fig. 21. Impact of dynamic interference.

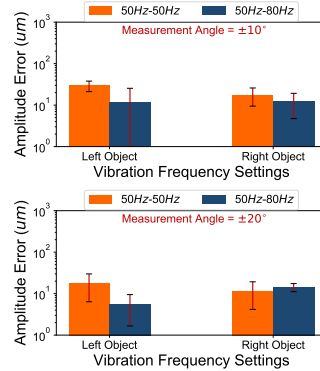


Fig. 22. Multi-object measurement.

6.3.3 Impact of dynamic interference

Then, we explore the ability of mmVib to deal with dynamic interference. In the 100cm-50Hz-100 μm setup, we let a person walking in other range bins, in the same range bin as the vibrating object, or in front of the radar to block the LOS path, respectively. The amplitude and frequency errors in Fig. 21 show that mmVib effectively resists the dynamic interference from NLOS paths, especially the case of walking in other range bins, whose median amplitude and frequency errors are 4.774 μm and 0.01454Hz. Moreover, we find that increasing the number of walking people does not significantly reduce the performance, as long as they are not obstructing the LOS path or very close to the vibrating object. Thus, mmVib's performance against the dynamic interference mainly depends on the relative positions of dynamic objects and the vibrating object.

6.3.4 Multi-object measurement

Next, we explore the ability of mmVib to measure multiple vibrating objects simultaneously. We place two identical calibrators symmetrically on the front left and front right of the radar, i.e., in the same range bin, and keep their vibrating directions along the radar's norm direction. Their measurement angles change from $\pm 10^\circ$ to $\pm 20^\circ$ to represent the near and far cases. We keep the vibration parameters of the left object as 50Hz-100 μm and change those of the right object from 50Hz-100 μm to 80Hz-100 μm to see the impact of vibrating frequencies on the signal separation. The reason for only using two vibrating objects while changing their spanning angle to evaluate the multi-object measurement's performance is that the spanning angle actually determines the quality of the spectrum analysis [22]. By finding the minimum spanning angle, we can estimate the maximum number of objects that can be simultaneously monitored within the range of the radar's field of view.

The results in Fig. 22 suggest that (i) mmVib can correctly separate vibration signals from multiple vibrating objects, but the measurement accuracy is limited by the angular resolution determined by the array size of the commercial mmWave radar; (ii) when the objects are farther from each other or their vibrating frequencies are different, the multi-object measurement achieves higher accuracy. Nevertheless, if we further reduce the spanning angle between two vibrating objects in the same bin, e.g., around $\pm 5^\circ$, the imageries of the two objects in the RAS closed to each other and the

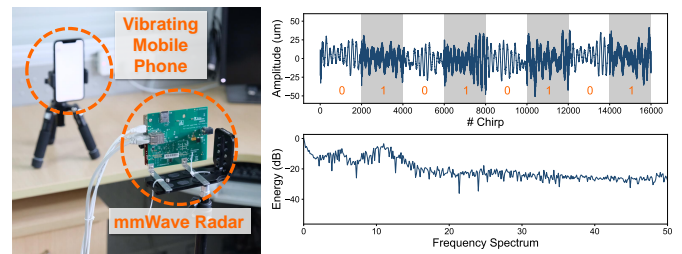


Fig. 23. Measuring the vibration of a mobile phone

signals extracted from them are twisted with each other. Therefore, the multi-object measurement's performance is mainly determined by the angular resolution mentioned in §4.3. The mmWave radar with a larger-size array is a better choice to measure more vibrating objects simultaneously.

6.3.5 Vibration measurement of daily objects

Last, we explore the ability of mmVib to measure the vibrations of daily objects. As shown in Fig. 23(a), we mount a mobile phone on a tripod in front of the radar with a measurement distance of 50cm. The mobile phone is programmed to vibrate with a period of 2s with a 50% duty cycle. Fig. 23(b) shows the time-domain signal as well as the frequency-domain signal measured by mmVib. We can clearly separate the vibration-off state (denoted by "0") and vibration-on state (denoted by "1") by exploring their different signal patterns. Therefore, this experiment shows that mmVib can measure the vibrations of daily objects.

6.4 Field Study

We conduct a field study to deploy and evaluate mmVib in a real-world steel plant. Fig. 24 shows the deployment, where the vibrating objects are the bearings of a transmission system containing the descaling pump, speed reducer, and main motor. The system works in two modes: low-speed and high-speed operation, with different rotating frequencies and μm -level amplitudes. The plant installs the piezoelectric vibration sensors on different parts of the target devices, and the sensor readings sent back to the console of the monitoring room via wires are used as the ground truth. To reduce the negative impact of ground vibrations, we can mount the mmWave radar on a tripod with an anti-vibration tripod head (Fig. 24) or on the pillar where ground vibrations have relatively low energy. Moreover, we have recently found that the signal changes caused by ground vibrations do not necessarily aggravate the negative impacts. How to exploit the information contained in them to improve the measurement accuracy may be an interesting and significant problem to study. The two factors, measurement distance and multi-object measurement, are considered in the following field-study evaluations.

Non-contact measurement: mmVib outperforms conventional approaches due to its non-contact measurement mechanism without any disturbance on the running machines or extra deployment overhead. Thus, we are most curious about whether it works in practice and how far the measurement distance can be. Fig. 25 shows the estimation stability (median and quartiles) and accuracy of the vibration amplitude and frequency of a descaling pump in two



(a) Non-contact measurement

(b) Multi-object measurement

Fig. 24. Field study of mmVib

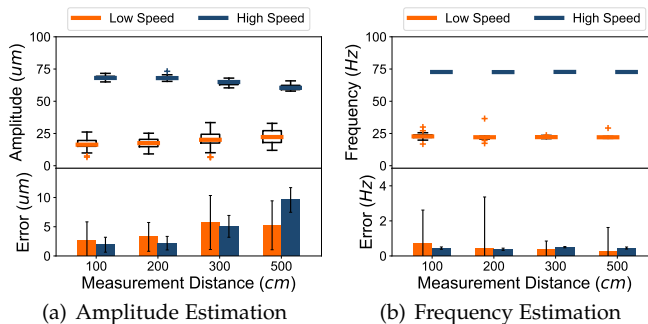


Fig. 25. Non-contact measurement results

operation modes. Taking the high-speed mode for example, when the distance varies from 100cm to 500cm , the average amplitude errors are $2.026\mu\text{m}$, $2.118\mu\text{m}$, $5.379\mu\text{m}$, $9.302\mu\text{m}$, respectively, while the average frequency errors are less than 0.5Hz . This indicates that mmVib can sense the μm -level vibration in practice, and its measurement is accurate and consistent when the distance $\leq 3\text{m}$. Although the measurement distance of 3m is enough for industrial applications, we believe that using TX-beamforming radar with a larger-size antenna array or adopting the state-of-the-art mmWave backscatter technology [21] can further improve the range.

Multi-object measurement: The second appealing characteristic of mmVib is its capability of measuring multiple vibrating objects simultaneously. In this experiment, we place the radar in front of the speed reducer and main motor and ensure that these two machines' bearings fall into different range bins. Fig. 26 shows that: (i) mmVib captures the fact that, although the amplitudes of the speed reducer and main motor differ from each other, their frequencies are nearly identical due to their direct connection (ii) The relatively small inter-quartile ranges and acceptable estimation errors demonstrate the stability and accuracy of mmVib for multi-object measurement.

7 CONCLUSION

In this paper, we present mmVib for μm -level vibration measurement. With the concept of MSC, mmVib adopts the multi-chirp property to improve VSNR and reduce the measurement error and utilizes the multi-antenna property to separate vibrations signals of multiple vibrating objects. Our evaluations show that mmVib works well in the laboratory as well as the field environment.

REFERENCES

- [1] Banner. Wireless Vibration Solution. <https://www.bannerengineering.com/be/en/solutions/iiot-data-driven-factory/vibration-monitoring-for-predictive-maintenance.html>, 2020.
- [2] S. Bi, X. Gao, V. M. Lubecke, O. Boric-Lubecke, D. Matthews, and X. L. Liu. A Multi-Arc Method for Improving Doppler Radar-Motion Measurement Accuracy. In *2018 IEEE/MTT-S International Microwave Symposium-IMS*, pages 244–247. IEEE, 2018.
- [3] E. P. Carden and P. Fanning. Vibration based Condition Monitoring: A Review. *Structural health monitoring*, 3(4):355–377, 2004.
- [4] L. Ding, M. Ali, S. Patole, and A. Dabak. Vibration Parameter Estimation using FMCW Radar. In *Proceedings of IEEE ICASSP*, pages 2224–2228, 2016.
- [5] S. W. Doebling, C. R. Farrar, M. B. Prime, and D. W. Shevitz. Damage Identification and Health Monitoring of Structural and Mechanical Systems from Changes in Their Bibration Characteristics: A Literature Review. Technical report, Los Alamos National Lab., NM (United States), 1996.
- [6] W. Gander, G. H. Golub, and R. Strebel. Least-Squares Fitting of Circles and Ellipses. *BIT Numerical Mathematics*, 34(4):558–578, 1994.
- [7] F. Guidi, A. Guerra, and D. Dardari. Personal Mobile Radars with Millimeter-Wave Massive Arrays for Indoor Mapping. *IEEE Transactions on Mobile Computing*, 15(6):1471–1484, 2015.
- [8] W. Jiang, C. Miao, F. Ma, S. Yao, Y. Wang, Y. Yuan, H. Xue, C. Song, X. Ma, D. Koutsonikolas, et al. Towards Environment Independent Device Free Human Activity Recognition. In *Proceedings of ACM MobiCom*, pages 289–304, 2018.
- [9] C. R. Karanam, B. Korany, and Y. Mostofi. Tracking from One Side: Multi-Person Passive Tracking with WiFi Magnitude Measurements. In *Proceedings of ACM/IEEE IPSN*, pages 181–192, 2019.
- [10] Keyence. Keyence Eddy-Current Displacement Sensor. https://www.keyence.com/ss/products/measure/measurement_library/type/inductive/, 2020.
- [11] Keyence. Laser Displacement Sensors. <https://www.keyence.com/products/measure/laser-1d/>, 2020.
- [12] D. K. Kim and Y. Kim. Quadrature Frequency-Group Radar and its Center Estimation Algorithms for Small Vibrational Displacement. *Scientific reports*, 9(1):1–17, 2019.
- [13] P. Li, Z. An, L. Yang, and P. Yang. Towards Physical-Layer Vibration Sensing with RFIDs. In *Proceedings of IEEE INFOCOM*, pages 892–900, 2019.
- [14] J. Lien, N. Gillian, M. E. Karagozler, P. Amihood, C. Schwesig, E. Olson, H. Raja, and I. Poupyrev. Soli: Ubiquitous Gesture Sensing with Millimeter Wave Radar. *ACM Transactions on Graphics*, 35(4):142, 2016.
- [15] C. X. Lu, S. Rosa, P. Zhao, B. Wang, C. Chen, N. Trigoni, and A. Markham. See through Smoke: Robust Indoor Mapping with Low-Cost mmWave Radar. In *Proceedings of ACM MobiSys*, 2020.
- [16] I. V. Mikkelson, S. Bakhtiari, T. W. Elmer, A. V. Sahakian, et al. Remote Sensing of Heart Rate and Patterns of Respiration on a Stationary Subject Using 94GHz Millimeter-Wave Interferometry. *IEEE Transactions on Biomedical Engineering*, 58(6):1671–1677, 2011.
- [17] I. Pefkianakis and K.-H. Kim. Accurate 3D Localization for 60GHz Networks. In *Proceedings of ACM SenSys*, pages 120–131, 2018.
- [18] S. Sami, Y. Dai, S. R. X. Tan, N. Roy, and J. Han. Spying with Your Robot Vacuum Cleaner: Eavesdropping via LiDAR Sensors. In *Proceedings of ACM SenSys*, pages 354–367, 2020.
- [19] L. Scalise, Y. Yu, G. Giuliani, G. Plantier, and T. Bosch. Self-Mixing Laser Diode Velocimetry: Application to Vibration and Velocity Measurement. *IEEE Transactions on Instrumentation and Measurement*, 53(1):223–232, 2004.
- [20] K. Siddiq, M. K. Hobden, S. R. Pennock, and R. J. Watson. Phase

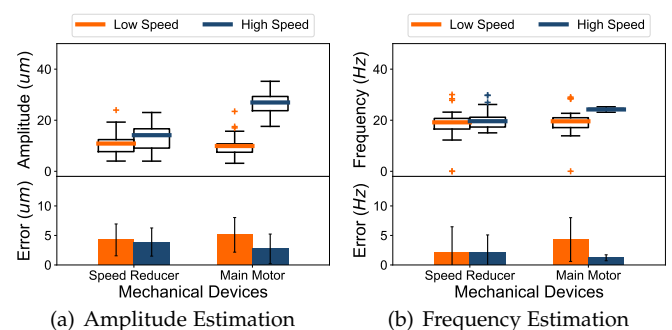
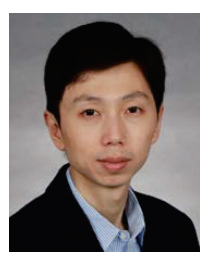


Fig. 26. Multi-object measurement results

- Noise in FMCW Radar Systems. *IEEE Transactions on Aerospace Electronic Systems*, 55(1):70–81, 2019.
- [21] E. Soltanaghaei, A. Prabhakara, A. Balanuta, M. Anderson, J. M. Rabaey, S. Kumar, and A. Rowe. MilliMetro: mmWave Retro-Reflective Tags for Accurate, Long Range Localization. In *Proceedings of ACM MobiCom*, pages 1–13, 2021.
- [22] P. Stoica, R. L. Moses, et al. *Spectral Analysis of Signals*. Pearson Prentice Hall Upper Saddle River, NJ, 2005.
- [23] TI. Introduction to mmWave Sensing: FMCW Radars. <https://training.ti.com/intro-mmwave-sensing-fmcw-radars-module-1-range-estimation>, 2020.
- [24] TI. IWR1642: Single-Chip 76GHz to 81GHz mmWave Sensor Integrating DSP and MCU. <http://www.ti.com/product/IWR1642>, 2020.
- [25] F. Tonolini and F. Adib. Networking across Boundaries: Enabling Wireless Communication through the Water-Air Interface. In *Proceedings of ACM SIGCOMM*, pages 117–131, 2018.
- [26] D. Tse and P. Viswanath. *Fundamentals of Wireless Communication*. Cambridge university press, 2005.
- [27] Z. Wang, Z. Chen, A. D. Singh, L. Garcia, J. Luo, and M. B. Srivastava. UWHear: Through-Wall Extraction and Separation of Audio Vibrations Using Wireless Signals. In *Proceedings of ACM SenSys*, pages 1–14, 2020.
- [28] T. Wei, S. Wang, A. Zhou, and X. Zhang. Acoustic Eavesdropping through Wireless Vibrometry. In *Proceedings of ACM MobiCom*, pages 130–141, 2015.
- [29] T. Wei and X. Zhang. mTrack: High-Precision Passive Tracking Using Millimeter Wave Radios. In *Proceedings of ACM MobiCom*, pages 117–129, 2015.
- [30] B. Xie, J. Xiong, X. Chen, and D. Fang. Exploring Commodity RFID for Contactless Sub-Millimeter Vibration Sensing. In *Proceedings of ACM SenSys*, pages 15–27, 2020.
- [31] C. Xu, Z. Li, H. Zhang, A. S. Rathore, H. Li, C. Song, K. Wang, and W. Xu. WaveEar: Exploring a mmWave-based Noise-Resistant Speech Sensing for Voice-User Interface. In *Proceedings of ACM MobiSys*, pages 14–26, 2019.
- [32] L. Yang, Y. Li, Q. Lin, H. Jia, X.-Y. Li, and Y. Liu. Tagbeat: Sensing Mechanical Vibration Period with COTS RFID Systems. *IEEE/ACM Transactions on Networking*, 25(6):3823–3835, 2017.
- [33] Z. Yang, P. H. Pathak, Y. Zeng, X. Liran, and P. Mohapatra. Vital Sign and Sleep Monitoring Using Millimeter Wave. *ACM Transactions on Sensor Networks*, 13(2):1–32, 2017.
- [34] Y. Zhang, G. Laput, and C. Harrison. Vibrosight: Long-Range Vibrometry for Smart Environment Sensing. In *Proceedings of ACM UIST*, pages 225–236, 2018.
- [35] Y. Zhu, Y. Yao, B. Y. Zhao, and H. Zheng. Object Recognition and Navigation Using A Single Networking Device. In *Proceedings of ACM MobiSys*, pages 265–277, 2017.
- [36] Y. Zhu, Y. Zhu, B. Y. Zhao, and H. Zheng. Reusing 60GHz Radios for Mobile Radar Imaging. In *Proceedings of ACM MobiCom*, pages 103–116, 2015.



Junchen Guo is a Ph.D. student at the School of Software, Tsinghua University. He received his B.E. degree in Computer Science and Technology at University of Science and Technology of China in 2016. His research interests include Internet of Things, wireless sensing, and networked systems. He is a student member of the IEEE and the ACM.



Yuan He is an associate professor in the School of Software and BNRIst, Tsinghua University. He received his B.E. degree in the University of Science and Technology of China, his M.E. degree in the Institute of Software, Chinese Academy of Sciences, and his Ph.D. degree in Hong Kong University of Science and Technology. His research interests include wireless networks, Internet of Things, pervasive and mobile computing. He is a member of the IEEE and ACM.



Chengkun Jiang received the B.E. degree in computer science from University of Science and Technology of China, Hefei, China, in 2015, and the Ph.D. degree in Software Engineering from Tsinghua University, Beijing, China, in 2020. In 2020, he joined Huawei Technology Co., Ltd., Shanghai, where he is currently a Principal Engineer in NFV Research Department, Cloud Core Network. His research interests include wireless sensing and 5G core architecture.



Meng Jin is currently an assistant professor at School of Electronic Information and Electrical Engineering, Shanghai Jiao Tong University. She is previously a post-doctoral researcher at School of Software and BNRIst, Tsinghua University. She received the B.S., M.S. and Ph.D. degrees in Computer Science from Northwest University, Xi'an, China, in 2012, 2015, and 2018, respectively. Her main research interests include Internet of Things, backscatter communication, and wireless sensing.



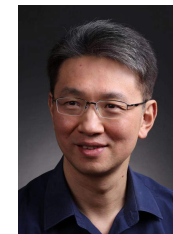
Shuai Li is currently a Master student at the School of Software, Tsinghua University. He received the B.E. degree in Software Engineering at Tsinghua University in 2020. His research interests include Internet of Things and wireless sensing. He is a student member of the IEEE.



Jia Zhang received the B.E. degree in the School of Software from Tsinghua University in 2019. He is currently a Ph.D. student in Tsinghua University. His research interests include Internet of Things and wireless sensing. He is a student member of the IEEE and the ACM.



Rui Xi is currently a post-doctoral researcher at School of Software and BNRIst, Tsinghua University. He received the M.S. and Ph.D. degrees in Computer Science from University of Electronic Science and Technology of China, Chengdu, China, in 2014 and 2019, respectively. His main research interests including Internet of Things, wireless sensing and AI. He is a member of the IEEE and the ACM.



Yunhao Liu received his B.S. degree in Automation Department from Tsinghua University, and an M.A. degree in Beijing Foreign Studies University, China. He received an M.S. and a Ph.D. degree in Computer Science and Engineering in Michigan State University, USA. He is now a professor at Automation Department and Dean of the GIX in Tsinghua University, China. He is a Fellow of IEEE and ACM.